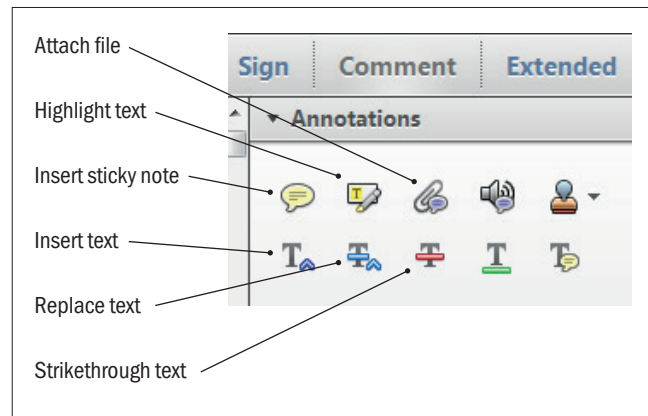


Making corrections to your proof

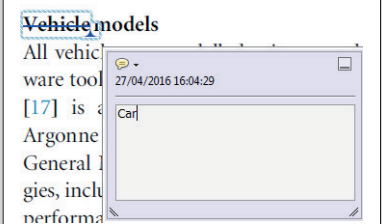
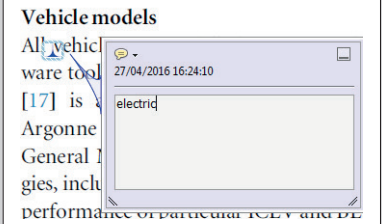
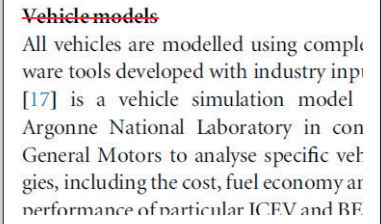
Please follow these instructions to mark changes or add notes to your proof. You can use Adobe Acrobat Reader (download the most recent version from <https://get.adobe.com>) or an open source PDF annotator.

The tools you need to use are contained in **Annotations** in the **Comment** toolbar. You can also right-click on the text for several options. The most useful tools have been highlighted here. If you cannot make the desired change with the tools, please insert a sticky note describing the correction.

Please ensure all changes are visible via the 'Comments List' in the annotated PDF so that your corrections are not missed.



Do not attempt to directly edit the PDF file as changes will not be visible.

<p>Replacing text</p> <p>To replace text, highlight what you want to change then press the replace text icon, or right-click and press 'Add Note to Replace Text', then insert your text in the pop up box. Highlight the text and right click to style in bold, italic, superscript or subscript.</p>	
<p>Inserting text</p> <p>Place your cursor where you want to insert text, then press the insert text icon, or right-click and press 'Insert Text at Cursor', then insert your text in the pop up box. Highlight the text and right click to style in bold, italic, superscript or subscript.</p>	
<p>Deleting text</p> <p>To delete text, highlight what you want to remove then press the strikethrough icon, or right-click and press 'Strikethrough Text'.</p>	
<p>Highlighting text</p> <p>To highlight text, with the cursor highlight the selected text then press the highlight text icon, or right-click and press 'Highlight text'. If you double click on this highlighted text you can add a comment.</p>	

QUERY FORM

JOURNAL: The Astrophysical Journal

AUTHOR: Boada et al.

TITLE: High Confidence Optical Confirmations among the High Signal-to-noise *Planck* Cluster Candidates

ARTICLE ID: apjaaf3a0

The layout of this article has not yet been finalized. This proof may contain columns that are not fully balanced/matched or other typographical imperfections; these issues will be resolved once the final corrections have been incorporated.

Please check that the **names of all authors as displayed in the proof are correct**, and that all **authors are linked to the correct affiliations**. Please also confirm that the correct corresponding author has been indicated. **Note that this is your last opportunity to review and amend this information before your article is published.**

If you have an Acknowledgments section, please check that the information there is complete and correct and that all relevant institutions, grant numbers, programs, and collaborators are mentioned as appropriate.

We have been provided with ORCID iDs for the authors as below. Please confirm whether the numbers are correct.

Steven Boada 0000-0002-0307-8693



John P. Hughes 0000-0002-8816-6800

Peter Doze 0000-0002-2408-0813

L. Infante 0000-0001-8581-932X

Page 2

Q1

Please define the acronym “SNR.” If it refers to “signal-to-noise ratio,” it must be updated to “S/N” throughout.

Page 13

Q2

Please check the details for any journal references that do not have a link; please update with correct details and supply a CrossRef DOI or NASA ADS link if available.

Page 13

Q3

Please provide the title for the code in reference [Bertin & Emmanuel 2011].

Page 13

Q4

Reference [Böhringer et al. 2000] is repeated, so we have deleted the latter instance. Please check.

Page 13

Q5

Please provide the publisher details in reference [Harris et al. 1990].

Page 14

Q6

In the references [Sunyaev & Zeldovich 1972, Tody 1993, Voges et al. 2000], please provide volume or page number, as needed.



High Confidence Optical Confirmations among the High Signal-to-noise *Planck* Cluster Candidates

Steven Boada¹ , John P. Hughes¹ , Felipe Menanteau^{2,3}, Peter Doze¹ , L. Felipe Barrientos⁴, and L. Infante⁴

¹Department of Physics and Astronomy, Rutgers, the State University of New Jersey, 136 Frelinghuysen Road, Piscataway, NJ 08854-8019, USA; boada@physics.rutgers.edu

²National Center for Supercomputing Applications, 1205 West Clark Street, Urbana, IL 61801, USA

³Department of Astronomy, University of Illinois at Urbana-Champaign, 1002 W. Green Street, Urbana, IL 61801, USA

⁴Instituto de Astrofísica y Centro de Astroingeniería, Facultad de Física, Pontificia Universidad Católica de Chile, Casilla 306, Santiago 22, Chile

Received 2018 September 14; revised 2018 November 16; accepted 2018 November 23; published 2018 MM DD

Abstract

We report on newly identified galaxy clusters from the high signal-to-noise ($>5\sigma$) end of the second all-sky *Planck* *Sunyaev–Zel'dovich* (SZ) catalog (PSZ2). The clusters are identified in deep, optical imaging from the Kitt Peak National Observatory 4 m Mayall telescope taken between 2014 and 2017. Here we focus on the highest richness systems, and identify galaxy clusters through a combination of the maxBCG algorithm and visual image inspection. Galaxy clusters are considered to be confirmed if they are both rich and spatially coincident ($\lesssim 6'$) with the reported PSZ2 position. Of the 85 fields containing unconfirmed PSZ2 candidates observed, we find 15 (17.6% of the observed sample) corresponding galaxy clusters ($0.13 < z < 0.78$), 12 of which are previously unrecognized as counterparts. To explain this low identification fraction, we consider three possible scenarios: that clusters are (1) mostly at *low-z*, (2) mostly at *high-z*, or (3) located in fields with high object density. None of these scenarios alone can account for the low purity of rich galaxy clusters among the high signal-to-noise PSZ2 unconfirmed candidates.

Key words: cosmology: observations – galaxies: clusters: general

1. Introduction

Galaxy clusters, especially massive clusters, are extraordinary objects that contain vital clues to the structure and evolution of the universe. The generally accepted Λ CDM cosmological model makes detailed predictions about the number and total mass distribution of galaxy clusters throughout the universe. These galaxy clusters, particularly at high redshift, play a crucial role in constraining large-scale structure formation and evolution from measurements of the overall matter density and the amplitude of matter fluctuations (e.g., Evrard 1989; Henry & Arnaud 1991; White et al. 1993a, 1993b; Eke et al. 1996; Donahue et al. 1998; Borgani et al. 2001), the dark energy equation of state (e.g., Henry 2004; Mantz et al. 2008; Vikhlinin et al. 2009), and the potential falsification of Λ CDM from the existence of extreme clusters (e.g., Mortonson et al. 2010; Harrison & Coles 2012; Harrison & Hotchkiss 2013; Waizmann et al. 2013).

Large-area sky surveys, both currently underway and planned, are identifying many tens of thousands of galaxy clusters for both detailed examinations of our cosmological models and as probes of fundamental physics. Clusters have been identified in numerous ways: as overdensities of galaxies in optical surveys (e.g., Abell 1958; Postman et al. 1996), as extended X-ray sources (e.g., Gioia et al. 1990; Ebeling et al. 1998; Böhringer et al. 2000), as clusters of mass in gravitational-weak-lensing surveys (e.g., Wittman et al. 2006), and most recently as “shadows” or “holes” in the cosmic microwave background (CMB). Today, a large number of galaxy clusters are being identified in ground-based, millimeter wave surveys conducted by the Atacama Cosmology Telescope (ACT; Swetz et al. 2011) and the South Pole Telescope (SPT; Carlstrom et al. 2011), among others. These surveys have identified hundreds of massive galaxy clusters up to redshifts of $z \sim 1.4$ (e.g., Menanteau et al. 2010b;

Vanderlinde et al. 2010; Marriage et al. 2011; Hasselfield et al. 2013; Bleem et al. 2015; Hilton et al. 2018). This detection approach exploits the cluster’s hot intracluster medium, which imprints a telltale signature on the CMB through the Sunyaev–Zel’dovich (SZ; Sunyaev & Zeldovich 1972) effect.

Deep, wide field photometric surveys such as the ongoing Hyper Suprime-Cam Survey (Aihara et al. 2018) and Dark Energy Survey (DES; The Dark Energy Survey Collaboration 2005), as well as future surveys like the Large Synoptic Survey Telescope (LSST; LSST Dark Energy Science Collaboration 2012), *Euclid*, and WFIRST will discover many thousands of additional galaxy clusters at redshifts to $z = 1$ (e.g., Dark Energy Survey Collaboration et al. 2016) and beyond. While a powerful discovery method, photometric surveys suffer from cosmological surface brightness dimming that reduces their sensitivity at high redshift (e.g., Calvi et al. 2014).

Using the SZ effect to discover clusters of galaxies has the distinct advantage that the surface brightness of the SZ effect does not dim with increasing redshift. This allows fairly homogeneous samples of massive clusters to be detected out to arbitrary distances. Now, *Planck* (Tauber et al. 2010; Planck Collaboration et al. 2011) has released an all-sky SZ sample (hereafter PSZ; Planck Collaboration et al. 2014, 2015a) that contains 1943 detections with 1330 confirmed clusters and another 613 (as of PSZ catalog⁵ versions 2.1 and 1) unconfirmed cluster candidates. Clusters were initially confirmed by cross-correlating with previous catalogs (see Section 4; Planck Collaboration et al. 2014). More recently, dedicated follow-up of still-unconfirmed clusters has begun in

⁵ http://szcluster-db.ias.u-psud.fr/sitools/client-user/SZCLUSTER_DATABASE/project-index.html

earnest (e.g., Liu et al. 2015; Planck Collaboration et al. 2015b, 2016; van der Burg et al. 2016; Burenin 2017; Amodeo et al. 2018; Barrena et al. 2018; Streblyanska et al. 2018).

This study was motivated by the release of the first PSZ all-sky catalog in 2013. We originally posited that the vast majority of the candidates must lie at $z > 0.4$ because the *Planck* confirmation process (Planck Collaboration et al. 2014) mostly relied on existing catalogs that have a preference for low- z clusters. Furthermore, the confirmed sample of the PSZ2 catalog has only a small fraction (3%) of $z > 0.6$ clusters compared to that expected ($\sim 20\%$) based on the theoretical halo mass function (e.g., Jenkins et al. 2001; Tinker et al. 2008) for a mass limit of $6 \times 10^{14} M_{\odot}$. Of particular interest to us is the search for the most massive clusters at high redshift, such as ACT-CL J0102-4915 (hereafter “El Gordo”), which weighs in at $\sim 2 \times 10^{15} M_{\odot}$ at a redshift of $z = 0.870$ (Menanteau et al. 2012). The Tinker halo mass function suggests as many as four clusters as massive as this at $z > 0.6$ in the full sky area covered by the *Planck* PSZ catalog (83.7% of the sky). If other clusters as massive as “El Gordo” exist, they are hiding as high-significance candidates within the objects in this all-sky catalog. In the discussion section below we examine this argument more carefully.

In this paper we report on our first efforts to classify unconfirmed PSZ cluster candidates using optical observations. This paper is organized as follows: Sections 2 through 4 describe the design, observations, data reduction and calibration, and creation of derived data products. In Section 5, we present the main results of our observations, and discuss those results in Section 6. In Section 7, we summarize the key results and conclude.

Unless otherwise noted, throughout this paper, we use a concordance cosmological model ($\Omega_{\Lambda} = 0.7$, $\Omega_m = 0.3$, and $H_0 = 70 \text{ km s}^{-1} \text{ Mpc}^{-1}$), assume a Chabrier initial mass function (Chabrier 2003), use AB magnitudes (Oke 1974), and quote uncertainties at the 1σ level.

2. Observational Strategy

The core of our observational design relies on the use of optical imaging to confirm the SZ detections as real clusters and provide photometric redshifts using the multicolor information. This design is based on the previous success with the ACT cluster confirmation process using 4 m class telescopes. Although *Planck*’s larger beam size (compared to both ACT and SPT) makes it more sensitive to clusters at lower redshifts (due to their larger projected area on the sky), among the confirmed clusters in the recently released all-sky *Planck* SZ catalog are the two highest significance high-redshift SZ detections from ACT (as well as several other ACT and SPT clusters).

Our strategy for this project is to use the Kitt Peak National Observatory (KPNO) Mayall-4 m telescope as the first and fundamental step to confirm the highest significance detections in the PSZ2 catalog that are visible across the entire northern sky. Optical imaging should be sufficient to confirm nearly all of the candidates. However, for the highest redshift candidates, near-IR imaging will be necessary. Those candidates with some evidence for a high- z brightest cluster galaxy (BCG) should be targeted with near-IR observations to confirm the presence of the BCG and to establish a red sequence of cluster members.

Following closely the procedure used for ACT follow-up (e.g., Menanteau et al. 2013), targets are prioritized by SZ

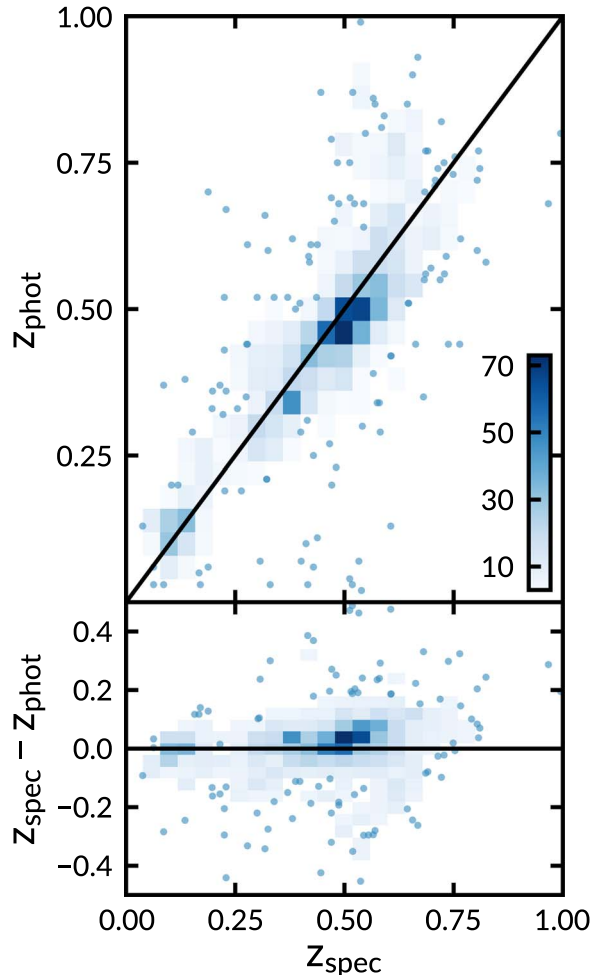


Figure 1. Comparison between photometric and spectroscopic redshifts for 1588 elliptical galaxies with spectroscopic redshifts from the SDSS. Top: the photometric redshifts are those reported by BPZ with a custom empirical prior on galaxy brightness for the photometric redshifts. Bottom: the difference between the spectroscopic and photometric redshifts, $z_{\text{spec}} - z_{\text{phot}}$, as a function of spectroscopic redshift. In both panels the shading scales (darker is greater) with the density of points where bins with fewer than three points are shown as single points. The solid black line shows the 1:1 relation.

We choose to initially report on targets with $\text{PSZ2 SNR} > 5$ as the statistical reliability of PSZ2 cluster candidates should be quite high: according to the *Planck* team $\sim 90\%$ of candidates at $\text{SNR} > 5$ are expected to be “real” clusters (see Figure 11; Planck Collaboration et al. 2015a).

2.1. Observations

All observations were conducted with the KPNO Mayall telescope. The optical observations were made with the MOSAIC camera mounted at the prime focus. Two detector packages were used for the observations. The earlier MOSAIC1.1 instrument consisted of eight 2048×4096 SITE CCDs, arranged 2×4 , separated by a gap ~ 50 pixels wide with a pixel scale of $0.^{\prime\prime}26 \text{ pixel}^{-1}$. MOSAIC1.1 was replaced with MOSAIC3, in mid-2015, and consists of four new $4k \times 4k$, 15 micron pixel, 500 micron thick LBNL deep-depletion CCDs. Because the only change from MOSAIC1.1 to MOSAIC3 are the CCDs and controllers, both versions have a $36' \times 36'$ field of view.

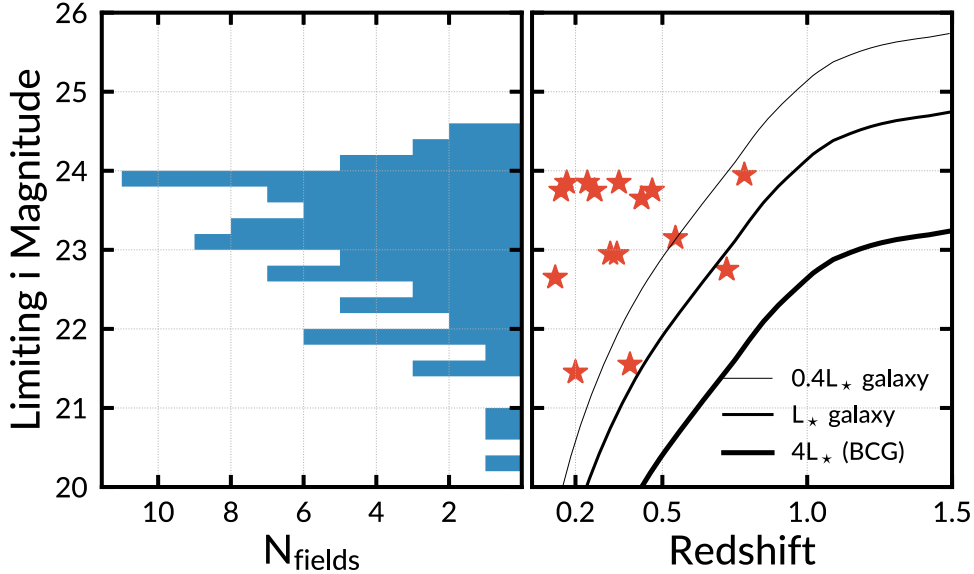


Figure 2. **Left:** histogram of the i -band magnitude corresponding to 80% completeness in galaxy recovery. When 80% completeness is not achieved we show the limiting magnitude with the highest completeness. **Right:** observed i -band magnitudes of L_* , $0.4L_*$, and $4L_*$ (BCG) early-type galaxies as a function of redshift. We define an L_* galaxy following Blanton et al. (2003) as a population of red galaxies at $z = 0.1$ and allow it to evolve passively. The orange stars indicate the field depths where we identify clusters and are plotted at the cluster's photometric redshift. The left and right panels can be combined to estimate the limiting redshift to which we could identify galaxy clusters.

Table 1
Summary of Cluster Confirmation

Cluster (1)	SNR (2)	PSZ2 (PSZ1) ID (3)	α (J2000) (4)	δ (J2000) (5)	Sep. (°) (6)	z_{cl} (7)	Ngal_c (8)	New (9)
PSZ2_G029.66–47.63	5.74	104	21:45:29.948	+21:43:26.35	4.73	0.32 ± 0.03	113	✓
PSZ2_G043.44–41.27	5.55	158	21:36:43.743	+10:19:02.08	1.24	0.43 ± 0.03	144	✓
PSZ2_G084.62–15.86	6.01	369 (284)	21:49:42.542	+33:09:17.54	1.13	0.27 ± 0.10	20	
PSZ2_G096.43–20.89	5.81	447	22:48:09.417	+35:33:49.30	0.49	0.35 ± 0.04	76	✓
PSZ2 G098.38+77.22	5.51	462 (346)	13:18:08.288	+38:30:19.96	5.84	0.78 ± 0.06	50 ^a	✓
PSZ2 G106.11+24.11	5.70	512	19:21:31.903	+74:33:27.01	0.51	0.15 ± 0.06	27	✓
PSZ2_G107.83–45.45	7.09	525	00:07:35.617	+16:07:02.15	0.83	0.55 ± 0.05	29	✓
PSZ2 G120.76+44.14	5.59	593	13:12:53.600	+72:55:05.85	2.02	0.34 ± 0.04	81	✓
PSZ2 G125.55+32.72	6.49	617	11:25:34.186	+83:58:55.65	1.44	0.20 ± 0.06	44	✓
PSZ2 G137.24+53.93	7.87	673	11:40:59.546	+61:07:07.07	4.61	0.47 ± 0.05	42	✓
PSZ2 G173.76+22.92	5.80	820	07:17:26.646	+44:05:02.73	1.62	0.13 ± 0.03	117	✓
PSZ2_G191.82–26.64	6.17	880 (646)	04:38:28.285	+04:37:19.82	5.18	0.17 ± 0.07	29	✓
PSZ2 G206.45+13.89	5.90	933 (682)	07:29:51.241	+11:56:31.49	1.97	0.39 ± 0.04	72 ^a	
PSZ2 G224.82+13.62	5.51	1009 (752)	08:01:41.492	-04:03:44.48	0.17	0.24 ± 0.04	55	
PSZ2 G305.76+44.79	5.72	1441 (1070)	12:59:53.623	-18:01:35.22	0.44	0.72 ± 0.07	58 ^a	✓

Notes. Column 1: the PSZ2 cluster name. Column 2: PSZ2 signal-to-noise ratio. Column 3: PSZ1 ID number. Column 4: BCG R.A. in J2000. Column 5: BCG decl. in J2000. Column 6: BCG separation from PSZ position in arcminutes. Column 7: cluster photometric redshift with 1σ uncertainty. Column 8: corrected number of member galaxies. Column 9: new confirmation?

^a Ngal_c should be taken as a lower limit. See Section 4.3 for details.

The optical observing strategy consists of targeted $griz$ observations of individual candidates with total exposure times of 360, 360, 1100, and 1100 s. The final exposures consist of four dithered positions with individual exposures of 90 s for the gr -bands or 275 s for the iz -bands. These exposure times are designed to ensure the unambiguous detection of the faint galaxies in the red cluster sequence up to $z \sim 1.0$ and of BCGs to higher redshifts. The choice of filters in our program is driven by the need to segregate early-type galaxies in the cluster through their colors (or photometric redshifts) by

sampling blueward and redward of the 4000 Å break over a broad range of redshifts.

3. Data Reduction and Calibration

Standard image reductions including subtraction of dark frames, flat-fielding, sky-subtraction, and bad pixel masking were performed by the National Optical Astronomy Observatory virtual observatory (VO) using the MOSAIC (Valdes & Swaters 2007) science pipelines. The resultant FITS files

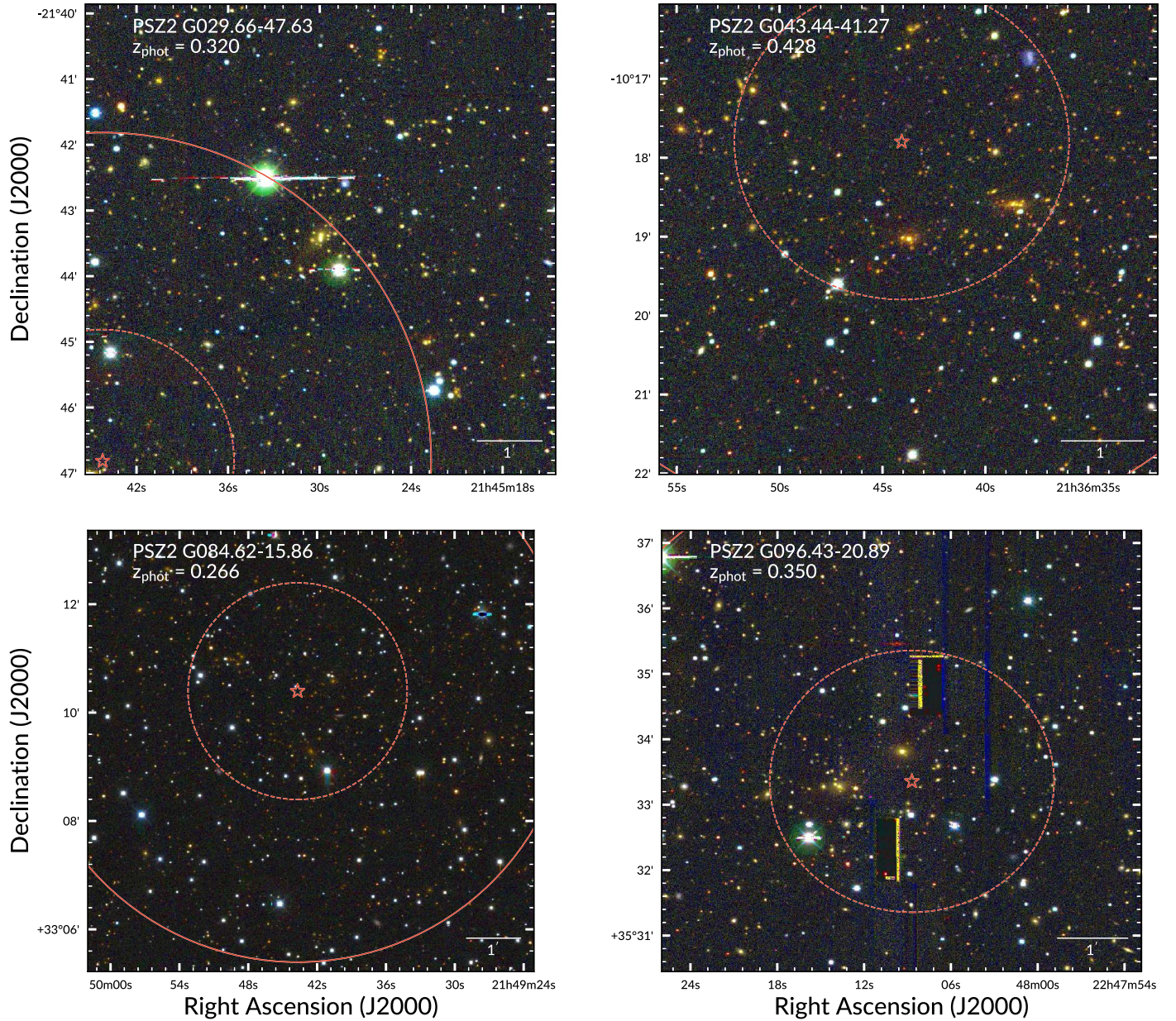


Figure 3. RGB (*irg*) color images for four PSZ clusters optically confirmed using our optical imaging. Each panel is centered on the cluster’s BCG and has a width of 1 Mpc at the corresponding cluster’s redshift. The horizontal bar in the lower right of each panel shows the scale of the panel, where north is up and east is to the left. The location of the PSZ detection is denoted by a red star. The dashed and solid, concentric, red circles are 2' and 5' in radius respectively.

consist of fully reduced images with either all single exposure CCDs mosaicked into a single image extension (as in the case of Mosaic1.1) or as a multi-extension FITS file with each single exposure CCD occupying a separate extension.

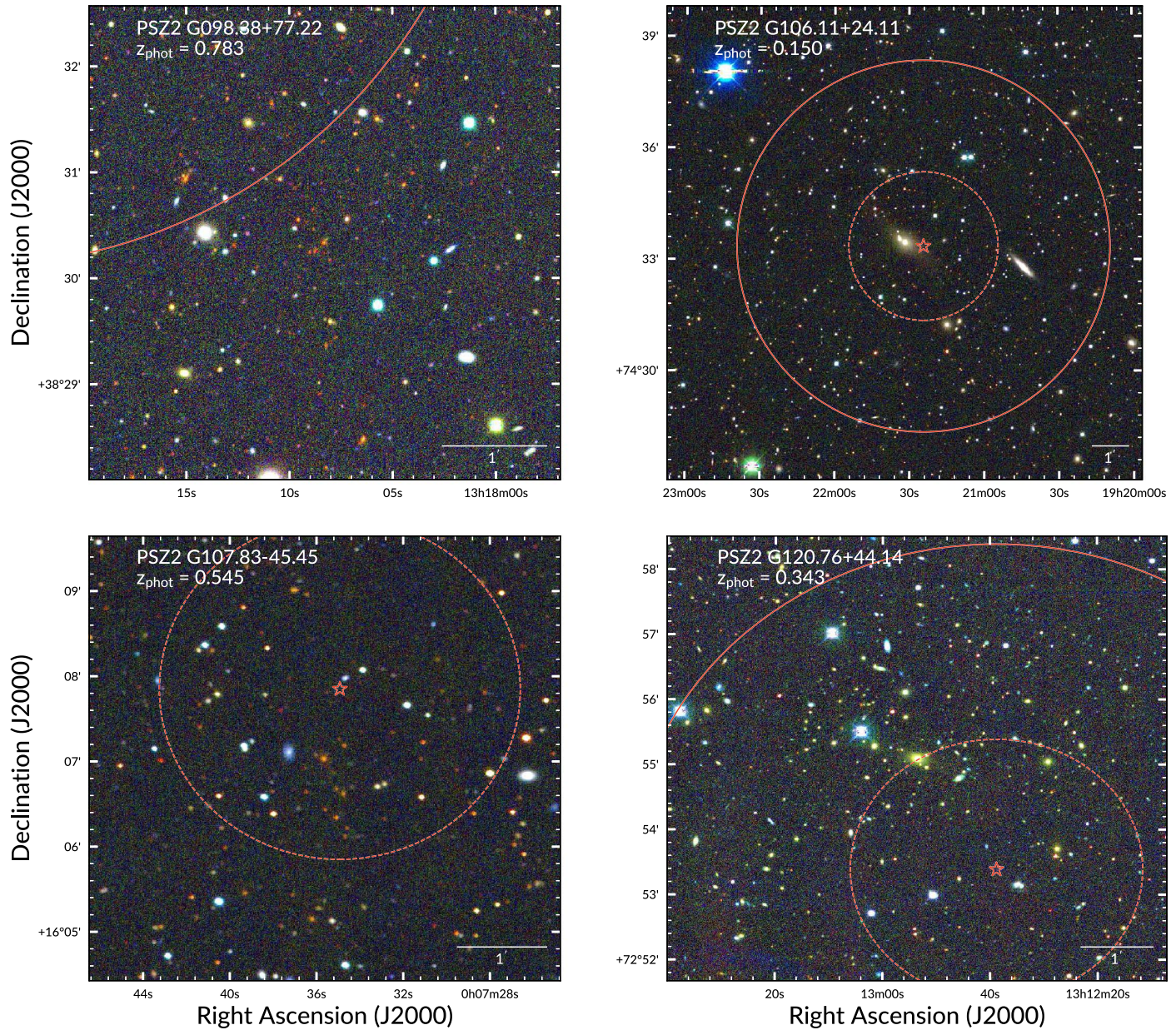
We then mosaic each separate exposure into a master mosaic as described in the following section.

3.1. Mosaicking

Combined mosaics are created with SWARP (version 2.38.0; Bertin et al. 2002). We create three distinct types of mosaics. The individual dither frames are stacked and then median combined to produce the final completed science mosaic. A “detection” is created by combining select science mosaics into a “chi2” image using a combination of the *i*- and *z*-bands, when both are available and of sufficient quality, or the *i*-band when

only one is present. Finally, we create a set of mosaics to produce the [three-color](#) image used for cluster finding. We median combine the *griz* science mosaics into “blue” (*g*-band), “green” (*r*-band), and “red” (*iz*-band) [mosaics](#). All final mosaics have a pixel scale of $0''.25 \text{ pixel}^{-1}$. The final exposure time is calculated as the median exposure time of the combined images, and similarly the final air mass is [the](#) median of the individual air masses. We also compute the final seeing for our mosaics by examining the mosaics with the IRAF (Tody 1993) task IMEXAMINE. Typical seeing is approximately $1''.2$ in the *i*-band.

Because of the different detector orientations, final science mosaics from images taken with Mosaic1.1 and Mosaic3 differ in size. Science mosaics are typically $\sim 0.45 \text{ degree}^2$ for observations taken with the Mosaic1.1 and $\sim 1.0 \text{ degree}^2$ for Mosaic3 observations.

**Figure 3.** (Continued.)

3.2. Source Extraction and Photometry

For source extraction and photometry estimation we use Source Extractor⁶ (hereafter SExtractor; version 2.19.5; Bertin & Arnouts 1996) run in dual image mode with the “chi2” detection image as the detection image (see Section 3.1). We configure SExtractor to detect objects with a minimum threshold of 1.5σ and a minimum area of 12 pixels. Our pipeline reports source photometry in magnitudes derived from summing the flux within the isophotal area reported by SExtractor. When the isophotal flux is flagged by SExtractor as unreliable, we fall back to magnitudes reported by SExtractor as MAG_AUTO with a Kron factor (Kron 1980) of 2.5 and a minimum radius of 3.5 pixels ($0.^{\prime\prime}88$).

Because our images are spread across the entire northern sky, we have implemented dust corrections for every source

across all four bands. This correction is particularly important in ensuring accurate galaxy colors and correct photometric redshifts. We utilize the infrared maps and correction routines provided by Schlegel et al. (1998) for this dust correction.

3.3. Astrometric Calibration

Each of the final science mosaics produced in the previous section is first astrometrically aligned with *Gaia* (Brown et al. 2016) Data Release 1 (Prusti et al. 2016) using SCAMP (Bertin 2006) as a part of PHOTOMETRYPipeline⁷ (PP; Mommerl 2017).

Sources are extracted from the mosaics with an SNR of at least 10 and with a minimum area of at least 12 pixels. The extracted sources are then matched to the *Gaia* data and a new astrometric solution is calculated. Matching all science images

⁶ <https://github.com/astromatic/sextarator>

⁷ <https://github.com/mommermi/photometrystreamline>

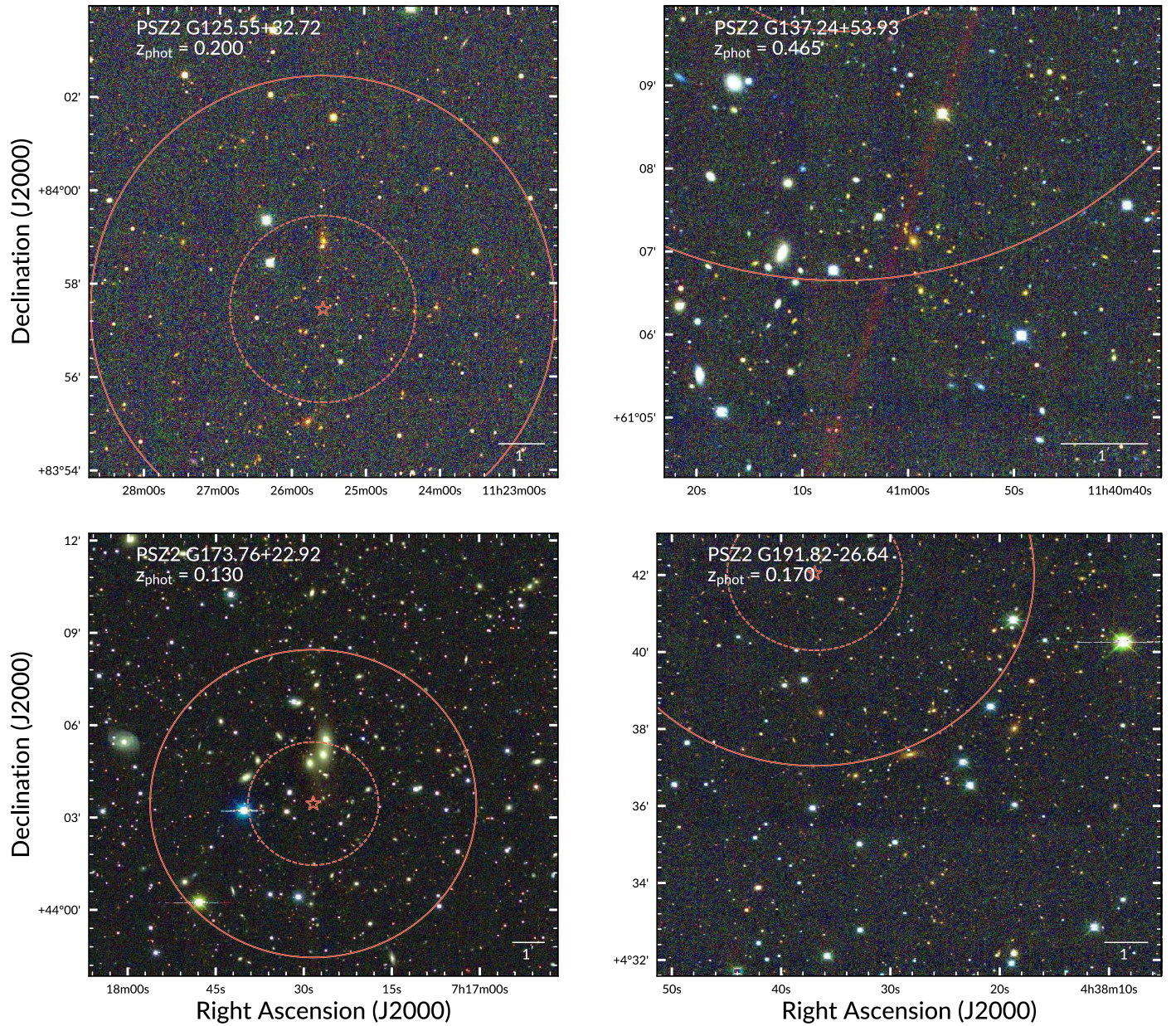


Figure 3. (Continued.)

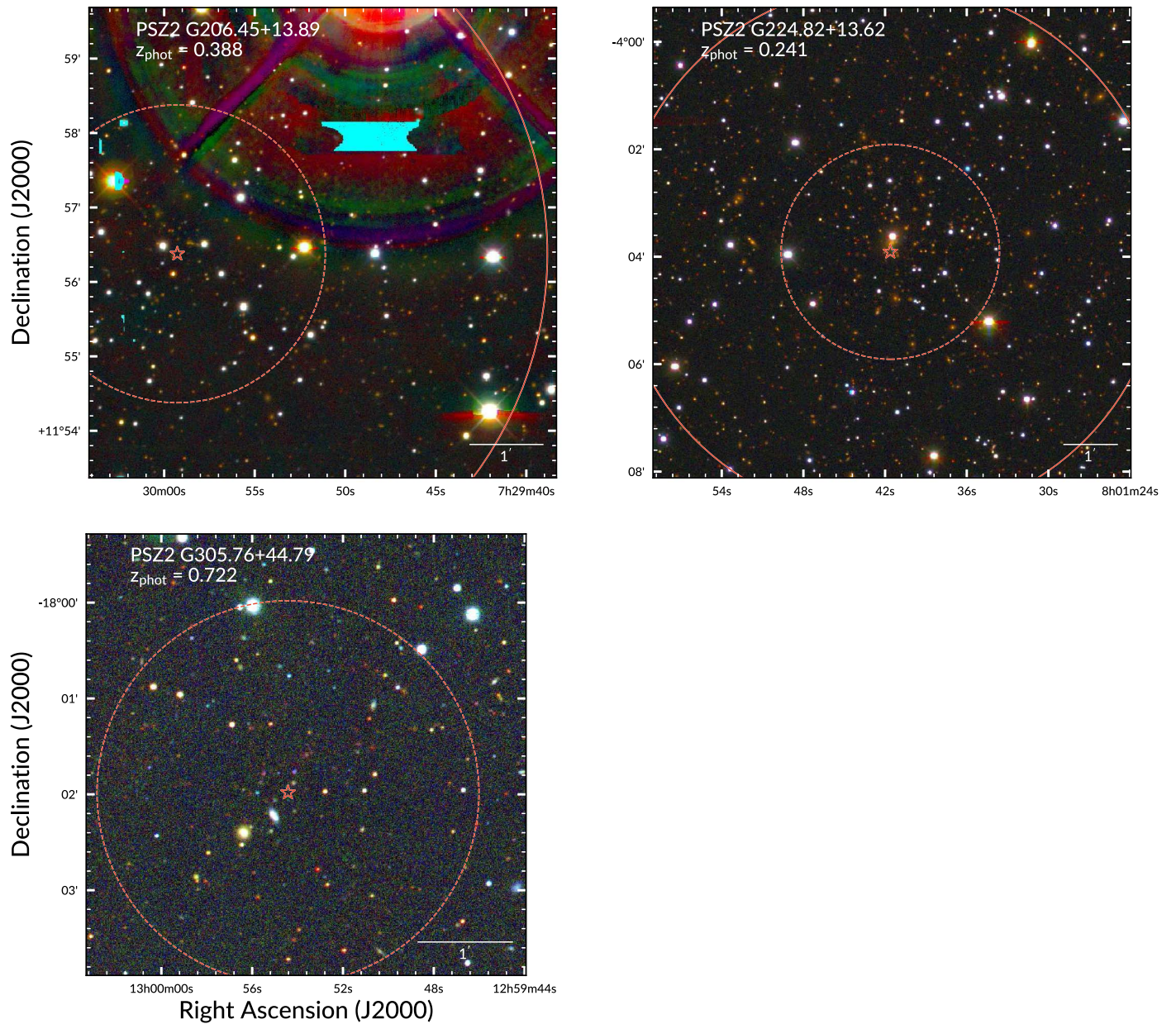
to the *Gaia* world coordinate system ensures that we have a common alignment across all observing runs. Because the initial astrometric solution from the VO is quite accurate, the typical root-mean-squared (rms) errors reported by SCAMP are less than 0''.05.

3.4. Photometric Calibration

After the mosaics have been astrometrically aligned, we use PP to produce a photometric solution. PP calculates a photometric zero-point in each of our observed bands by comparing field stars located throughout the science mosaic to known photometry from large-area sky surveys. Because our sources are spread across the entire northern sky, and because we prefer to minimize the number of differences between photometric solutions we are limited to two optical surveys. We first seek photometric data from the *Sloan Digital Sky*

Survey (SDSS; York et al. 2000) Data Release 13 (DR13; Albareti et al. 2017). When our target does not lie within the SDSS footprint we utilize the Panoramic Survey Telescope and Rapid Response System (Pan-STARRS; Chambers et al. 2016) Data Release 1 (hereafter PS1; Flewelling et al. 2016). Both surveys provide accurate *griz* magnitudes and large online queriable databases for rapid automated calibration.

Sources are extracted from the combined mosaics with a 3'' (12 pixel) diameter aperture; stars in our science images with $\text{SNR} \geq 10$ are matched to a survey catalog and a photometric zero-point is determined. Stars selected from the large-area sky surveys have either *r*-band (for PS1) or *g*-band (for SDSS) magnitudes < 21 and accurate catalog photometry (e.g., the “clean” SDSS flag). We use at least 50% of the available stars to derive the zero-point resulting in zero-points calculated from approximately 10–500 stars and with typical uncertainties of 0.05 mag for the *gri*-bands and 0.16 mag for the *z*-band.

**Figure 3.** (Continued.)

4. Analysis

4.1. Photometric Redshifts

We determine photometric redshifts (photo- z) from the four-band optical imaging catalogs using the Bayesian Photometric Redshifts (BPZ; Benitez 2000; Coe et al. 2006) code following the same procedure as that in Menanteau et al. (2009).

We assess the effectiveness of our photo- z estimates by comparing with the available spectroscopic redshifts (spec- z) from the SDSS. We use three diagnostics to gauge photo- z accuracy. First, we report the full scatter between the photo- z and spec- z , defined as:

$$\sigma_f = \text{rms}[\delta z / (1 + z_{\text{spec}})], \quad (1)$$

where $\delta z = z_{\text{spec}} - z_{\text{phot}}$. Second, we report the normalized median absolute deviation (NMAD; Ilbert et al. 2009; Dahlen

et al. 2013; Molino et al. 2017), given as

$$\sigma_{\text{NMAD}} = 1.48 \times \text{median} \left(\frac{|\delta z|}{1 + z_{\text{spec}}} \right), \quad (2)$$

which provides an estimate of the scatter resistant to catastrophic outliers. Finally, the catastrophic outlier fraction (OLF) where we define a catastrophic outlier (following Molino et al. 2017) as,

$$\eta = \frac{|\delta z|}{(1 + z_{\text{spec}})} > 5 \times \sigma_{\text{NMAD}}. \quad (3)$$

Figure 1 shows the photo- z performance as a function of the true spectroscopic redshift. Because we are primarily concerned with identifying clusters containing early-type galaxies, we show only galaxies classified E/S0 by BPZ. We find

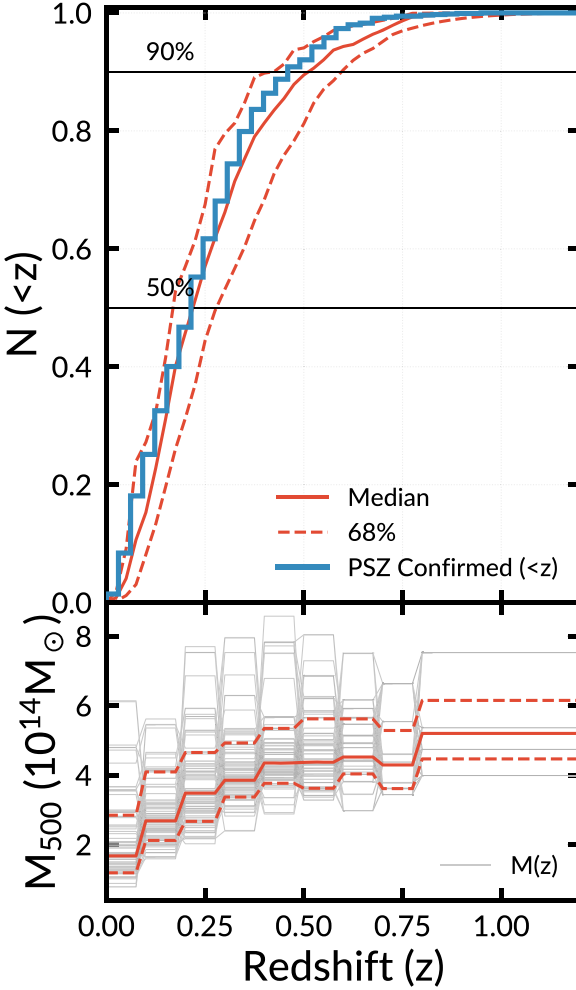


Figure 4. Top: the predicted number of clusters as a function of redshift and normalized to unity from the mass function of Tinker et al. (2008). At each redshift the lower mass limit is given by the mass in the bottom panel at the corresponding redshift. The blue PSZ confirmed curve shows the normalized, cumulative number of confirmed clusters as a function of redshift. For reference we show the 50% and 90% fractional completeness levels. Bottom: cluster mass as a function of redshift. Redshift bins are the same as Planck Collaboration et al. (2015a) Figure 27. In each panel the solid and dashed orange lines show the median and region enclosing 68% of the data respectively.

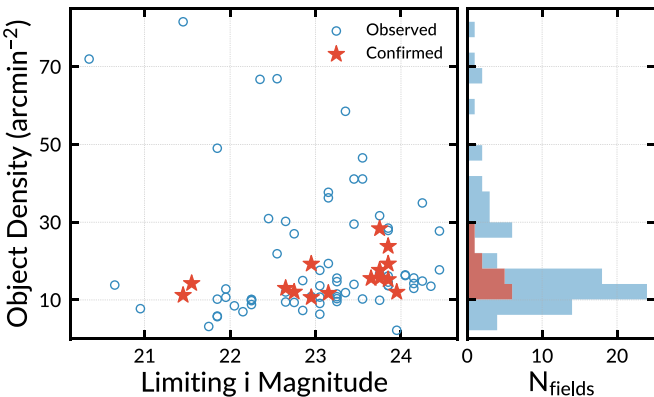


Figure 5. Right: object density in units of number per arcmin^{-2} as a function of the 80% i -band limiting magnitude taken from Figure 2. Fields where no cluster is identified are given by blue circles and fields with confirmed clusters are shown by orange stars. Left: histogram of the object surface density of observed fields.

$\sigma_f = 0.067$, $\sigma_{\text{NMAD}} = 0.048$, and an outlier fraction, $\eta = 0.9\%$.

4.2. Recovery of the Brightest Cluster Galaxies

We have designed our observations to detect BCGs to $z \sim 1.5$. To quantify the actual depths of our images, we perform two distinct tests. First, we perform a Monte Carlo simulation by injecting artificial, elliptical galaxies into the science imaging and computing their recovery fractions. Second, we fit a power-law model to the bright side of each field’s differential number count curve and identify the magnitude, m , at which the observed differential, dN/dm , falls below the extrapolated power-law fit by a specified amount.

The Monte Carlo simulation broadly follows the procedure given in Menanteau et al. (2010a). We create the artificial elliptical galaxies with the MODELING package, part of ASTROPY (The Astropy Collaboration et al. 2013). The synthetic galaxies are created to have de Vaucouleurs (de Vaucouleurs 1948) profiles and surface brightnesses corresponding to their magnitude and assumed sizes. We inject the artificial galaxies into our science images with similar noise characteristics as their real counterparts.

We generate 10 rounds each spreading 100 elliptical galaxies randomly across our science imaging. Galaxies are placed at different random positions, from round to round, to suppress abnormally boosted recovery fractions due to source confusion. The artificial galaxies have total fluxes corresponding to apparent magnitudes between 20 mag $< i <$ 25 mag with 0.2 mag spacing. We report the 80% i -band limit for each field, which is the magnitude where 80% of the simulated galaxies are recovered.

The second method to estimate the limiting magnitudes of our observations uses the calibrated SExtractor catalogs (see Section 3.2). We bin the objects identified by SExtractor as galaxies in 0.5 mag wide bins from $15 < i < 30$. We identify the peak of the differential number counts function (dN/dm versus m) in log space and fit a power-law model to the five magnitude bins on the bright side of the peak. The 80% completeness limit is defined as the magnitude bin at which the observed counts are 80% of the value from the extrapolated power law.

The completeness limits reported by each method are consistent and provide an important check on one another as they are wholly independent estimates of the limiting i -band magnitude in each of our fields. We choose to focus on the limiting magnitudes reported by the number counts based method as it is less prone to errors from very bright stars or diffuse emission from the Milky Way also present in some fields.

With a limiting magnitude reported for each field, we are able to estimate the redshift to which we could reliably identify massive galaxy clusters. We compare the completeness limits of our observations to the expected (i.e., known) apparent magnitudes of galaxies in clusters as a function of redshift. We define the expected apparent i -band magnitude of a galaxy following the population of red galaxies defined by Blanton et al. (2003). The $0.4L_*$, L_* , and $4L_*$ galaxies (representing faint members to bright BCGs) are composed of stars formed in a burst at $z = 5$, with solar metallicity (Bruzual & Charlot 2003), and allowed to evolve passively, $\tau = 1.0$ Gyr. We show the

expected i -band apparent magnitude as a function of redshift for each galaxy in the right panel of Figure 2.

4.3. Cluster Finding

In this section, we briefly describe the algorithms and methods used to select the galaxy clusters from the multi-wavelength optical imaging. We follow the methods described in detail in Menanteau et al. (2009, 2010b) and direct the reader there for an in-depth description and discussion of the methods. In short, we adopt a hybrid approach where we first manually identify (by eye) potential cluster BCGs and then use the maxBCG algorithm (Koester et al. 2007) to identify cluster members.

We first create a three-color image using STIFF (version 2.4.0; Bertin & Emmanuel 2011). The red, green, and blue channels are given by the corresponding combined mosaics described in Section 3.1. We then visually inspect an area of 6' in radius centered on the position of each unconfirmed PSZ detection. This search area should enclose the vast majority of clusters (e.g., Planck Collaboration et al. 2016; Streibyanska et al. 2018) and allows for the inclusion of possibly disturbed cluster systems (e.g., see Figure 10; Planck Collaboration et al. 2015a). This search radius, which is slightly larger than the expected positional uncertainty of *Planck* sources, will enable us to conduct a thorough search while still reporting high confidence confirmations. Potential BCGs are selected manually and are identified by their characteristic colors and accompanying member galaxies.

Once a potential BCG is selected, the maxBCG algorithm selects nearby member galaxies. We require these member galaxies to meet the following conditions: (1) they must be classified as either E or E/S0 type according to BPZ; (2) they must have $|z_{\text{BCG}} - z| < 0.05$ and be within a 1 Mpc projected radius of the BCG; (3) they must be fainter than the selected BCG and brighter than $0.4L_*$, where we have defined L_* in the previous section; and (4) they must have colors consistent with the cluster. To ensure the last point, we obtain a local color-magnitude relation for $g-r$ and $r-i$ and use a 3σ mean sigma-clipping method to iteratively remove galaxies that have colors beyond 3σ from the local color-magnitude relationship. The potential member galaxies are iterated over until the number of cluster members converges.

The photo- z 's of the galaxies are combined using the same 3σ mean sigma-clipping algorithm to estimate the cluster's mean redshift, z_{cl} . We use this cluster redshift measurement and the member selection criteria given previously to estimate the number of cluster members within 1 Mpc which we define as the richness (e.g., Abell 1958) of the cluster, Ngal . For three fields where we identify rich clusters, the depth of our imaging does not allow us to reliably detect galaxies to $0.4L_*$ at the redshift of the cluster. These clusters can be easily identified among the orange star points in the right panel of Figure 2. The richness estimates for these three fields, should, therefore, be taken as lower limits. We note these lower limits in Table 1 and in our discussion of individual clusters in Section 6.

We correct the Ngal estimate by subtracting a statistical background of galaxies. We select background galaxies using the same redshift, luminosity, and color criteria as the member galaxies described previously. However, to ensure that we are not including galaxies belonging to the cluster itself, we only consider galaxies beyond 3 Mpc of each cluster's position. The number of background galaxies is scaled by the ratio of areas

and then subtracted from the number of cluster members to provide a corrected Ngal , Ngal_c , which we then use to compute other important quantities. In practice the corrected number of galaxies is between 15% and 20% lower than the uncorrected number (Menanteau et al. 2010b). We report Ngal_c for the remainder of this work.

5. Results

Here, we report the high confidence clusters identified as a result of our cluster finding. A high confidence result consists of a clear BCG and many accompanying satellite galaxies (high richness). For the 85 fields observed, we identify 15 high confidence clusters (see Figures 3), including three clusters recently confirmed by others. We discuss all 15 clusters in detail below.

In the following subsections, we compare our results with previously known sources by querying the NASA/IPCA Extragalactic Database (NED)⁸ and the SIMBAD (Set of Identifications, Measurements, and Bibliography for Astronomical Data) astronomical database⁹ (Wenger et al. 2000). We include sources from the NRAO (National Radio Astronomy Observatory) Very Large Array Sky Survey (NVSS; Condon et al. 1998), the Röntgensatellit (ROSAT) All-Sky Survey Bright Source Catalog (RASS-BSC; Voges et al. 1999), the ROSAT All-Sky Faint Source Catalog (RASS-FSC; Voges et al. 2000), and the SDSS. We have included cross identifications with the all-sky galaxy cluster catalog from Wen et al. (2018) using the label WHY. We make note of confident associations of X-ray and radio sources with the BCG or other clusters members within 5' of the reported BCG pointing (within 10' for the three low redshift clusters).

5.1. PSZ2 G029.66–47.63

This is a rich cluster at $z_{\text{cl}} = 0.32 \pm 0.03$ with 113 members, approximately 5' to the northwest of the *Planck* position. The X-ray source 1RXS J214531.1–214339 as well as the catalogued system WHY J214529.9–214325 are positionally coincident with the BCG. Our data show another, slightly less rich, system (with $z_{\text{cl}} = 0.33 \pm 0.04$ and 76 members and with a BCG at $\alpha = 21:45:44.7$, $\delta = -21:47:01.5$) within 0.5' of the *Planck* position. Both systems likely contribute to the *Planck* SZ signal. This is the richest cluster in our sample.

5.2. PSZ2 G043.44–41.27

This is the richest cluster we have found; the system is at $z_{\text{cl}} = 0.43 \pm 0.03$ with 144 members. There are two plausible BCGs with nearly the same photo- z ; the one we select is slightly brighter in the i -band, yields a slightly higher number of cluster members, and is positionally coincident with the X-ray source 1RXS J213644.4–101904. The other bright galaxy is at $\alpha = 21:36:38.6$, $\delta = -10:18:35.7$, some 1.3' to the west. This galaxy is associated with a bright radio source (NVSS J213638–101836) with a flux density of 107.8 ± 3.3 mJy at 1.4 GHz that has been classified as a symmetric double (Douglas et al. 1996).

⁸ <https://ned.ipac.caltech.edu/>

⁹ <http://simbad.u-strasbg.fr/simbad/>

5.3. PSZ2 G084.62–15.86

This cluster was previously confirmed by the *Planck* team, where they quote a spectroscopic cluster redshift (from two members) of $z_{\text{spec}} = 0.364$ (Planck Collaboration et al. 2016). This system has at least three bright member galaxies within $2'$ of the *Planck* position that are plausible BCG candidates. Among these we chose the brightest one in the i -band (which is about an arcminute south of the *Planck* team’s chosen BCG) and recovered the cluster at $z_{\text{photo}} = 0.27 \pm 0.10$ with 20 members. The *Planck* team’s selected BCG is associated with a radio source (NVSS J214940+331031) with a flux density of 19.7 ± 0.8 mJy at 1.4 GHz.

5.4. PSZ2 G096.43–20.89

The BCG of this cluster is only $0.5'$ from the *Planck* position. The cluster’s redshift is $z_{\text{cl}} = 0.35 \pm 0.04$ with 76 members. An X-ray source (1RXS J224806.6+353230) is $1.44'$ away from the BCG position. This cluster appears to extend more toward the southwest quadrant in the direction of a cataloged Zwicky cluster (ZwCl 2245.6+3516; Zwicky & Kowal 1968). Cataloged cluster WHY J224809.4+353348 is positionally consistent with the BCG of our *Planck* confirmation.

5.5. PSZ2 G098.38+77.22

This field contains multiple clusters within $10'$ of the *Planck* candidate. The counterpart we have selected is the one that is closest to the *Planck* position and also has the highest N_{gal} value in our data. It also happens to be the highest redshift cluster in our full sample at $z_{\text{cl}} = 0.78 \pm 0.06$ with at least 50 members; it is $5.8'$ away from the *Planck* position. About $2'$ east of our chosen BCG there is a luminous ($i \sim 20$ mag), red galaxy (SDSS J131814.99+383055.8) with a spectroscopic redshift of $z = 0.726$. This galaxy has similar colors to the cluster BCG and may be part of the system. There are two other systems to comment on that are cataloged in NED as GMBCG J199.59552+38.43492 and WHL J131842.9+384300. GMBCG J199.59552+38.43492 is a rich system ($N_{\text{gal}} = 48$) at redshift $z_{\text{cl}} = 0.41 \pm 0.05$ that is located some $9'$ south of the *Planck* position. WHL J131842.9+384300 is not as rich ($N_{\text{gal}} = 23$) and not as distant ($z_{\text{cl}} = 0.17 \pm 0.05$), and is $8.6'$ north of the *Planck* position. Each of the BCGs in these clusters have spectroscopic redshifts (0.4193 and 0.2377) that are consistent with the values quoted from our photometry. It is possible that all of the clusters discussed here contribute to the reported SZ signal.

5.6. PSZ2 G106.11+24.11

PSZ2 G106.11+24.11 is a low redshift system at $z_{\text{cl}} = 0.15 \pm 0.06$. The BCG is a large galaxy close to the *Planck* position. There are 27 members after correcting for background galaxies. This object was identified as an X-ray cluster (RXC J1921.3+7433) based on its extent in the RASS (Böhringer et al. 2000), although these authors did not publish a redshift. Using their flux value and our photometric redshift, we estimate the cluster’s X-ray luminosity in the 0.1–2.4 keV band to be $L_X \sim 2.6 \times 10^{44}$ erg s $^{-1}$. This luminosity value is broadly consistent with those of other confirmed *Planck* clusters at this redshift range (Planck Collaboration et al. 2015b). We note that the cataloged cluster WHY J192115.0

+743114 is centered on a fainter member of our system some $2'$ south of the *Planck* position.

5.7. PSZ2 G107.83–45.45

This cluster at $z_{\text{cl}} = 0.55 \pm 0.05$ has 29 members. The BCG (SDSS J000735.62+160701.8) as well as another member (SDSS J000736.15+160508.9) have spectroscopic redshifts from the SDSS of $z = 0.5673$ and $z = 0.5667$, respectively. There are four other galaxies with SDSS spectroscopic redshifts (0.5649, 0.5661, 0.5655, and 0.5625) within $7'$ (2.7 Mpc) of the BCG.

5.8. PSZ2 G120.76+44.14

The BCG we select yields an estimated redshift for the cluster of $z_{\text{cl}} = 0.34 \pm 0.04$ with 81 members; this galaxy has a published spectroscopic redshift of $z = 0.2959$ (Huchra et al. 1990). We associate the cluster with A1705 and the RASS X-ray source 1RXS J131252.0+725514.

Approximately $2.6'$ south of the PSZ2 position, there is a luminous red galaxy with a gravitationally lensed arc that is the BCG of a rich system cataloged as WL 1312.5+7252 with a photometric redshift of 0.55 (Dahle et al. 2003). This galaxy is also a radio source (NVSS J131230+725051) with a flux density of 3.5 ± 0.5 mJy (1.4 GHz). Our analysis also yields a rich cluster with this BCG ($\alpha = 13:12:30.9$, $\delta = +72:50:54.2$) with $N_{\text{gal}} = 61$ at $z = 0.60 \pm 0.05$. Given the similar optical richnesses of these two systems it is likely that both contribute to the *Planck* SZ signal.

5.9. PSZ2 G125.55+32.72

There are two plausible BCGs in this cluster; the one we select yields a redshift of $z_{\text{cl}} = 0.20 \pm 0.06$ and 44 members. The other BCG ($\alpha = 11:25:46.8$, $\delta = +83:55:04.4$) is about 0.12 mag fainter in the i -band and, using it for cluster finding, results in a cluster at $z_{\text{cl}} = 0.20 \pm 0.05$ with 46 members. These two plausible BCGs are separated by $\sim 4'$. Both BCGs are radio sources: the northern galaxy (corresponding to our selected BCG) is cataloged as NVSS J112535+835858 with a 1.4 GHz flux density of 10.2 ± 0.9 mJy; the southern one corresponds to NVSS J112550+835508 with a flux density at the same frequency of 3.6 ± 0.6 mJy. The southern galaxy is about $1'$ away from the RASS X-ray source 1RXS J112547.3+835559. Both systems should contribute to the *Planck* SZ signal and the quoted richness in Table 1 is almost surely an underestimate of the richness of the combined system.

5.10. PSZ2 G137.24+53.93

Here we find a cluster at $z_{\text{cl}} = 0.47 \pm 0.05$ with 42 members. The BCG is a radio source (NVSS J114059+610658) with a flux density of 10.2 ± 0.9 mJy (1.4 GHz) and has a spectroscopic redshift from the SDSS of $z = 0.4770$. Another cluster member also has a concordant SDSS spectroscopic redshift of $z = 0.4697$. The cluster has been cataloged as WHL J114058.8+610631 with a similar photometric redshift. We note that the cataloged cluster GMBCG J175.54011+61.13607 is some $8.5'$ east of the *Planck* position. This is a low redshift system ($z_{\text{cl}} = 0.13 \pm 0.06$) with 20 members. It is disfavored as the counterpart given its large distance from the *Planck* position.

5.11. PSZ2 G173.76+22.92

This low redshift system, which we find at $z_{\text{cl}} = 0.13 \pm 0.03$, has a very interesting BCG. It is cataloged in NED as B3 0713+441 and has a spectroscopic redshift of $z = 0.0652$ (Bauer et al. 2000). It is also associated with the RASS X-ray source 1RXS J071726.9+440557 as well as a bright radio source (NVSS J071726+440504) with a flux density of 220.4 ± 7.6 mJy (at 1.4 GHz). Higher resolution images from Faint Images of the Radio Sky at Twenty-centimeters (Becker et al. 1995) reveal that this radio source is double lobed. Some 6' to the east is a cataloged Seyfert 1 galaxy (2MASX J07180060+4405271) with a spectroscopic redshift of $z = 0.0614$ (Michel & Huchra 1988) and a 1.4 GHz radio flux of 50.8 ± 1.6 mJy (NVSS J071800+440527). Our cluster is positionally coincident with WHY J071726.7+440502.

5.12. PSZ2 G191.82–26.64

This is another low redshift cluster at $z_{\text{cl}} = 0.17 \pm 0.07$ with 29 members. Two cluster members are associated with radio sources: NVSS J043836+043824 and NVSS J043818+043802 with 1.4 GHz flux densities of 24.8 ± 1.2 mJy and 22.7 ± 1.5 mJy, respectively.

5.13. PSZ2 G206.45+13.89

We find a cluster at $z_{\text{cl}} = 0.39 \pm 0.04$ with at least 72 cluster members. A bright star ($V = 4.5$ mag; Høg et al. 2000) lies only $\sim 4.9'$ away from the reported BCG, which prevents accurate photo-z estimates for a significant fraction of the projected area of the cluster. This cluster has been previously confirmed in Barrena et al. (2018) as a rich cluster with a spectroscopic redshift of $z_{\text{spec}} = 0.406$ from 45 members. We confirm the presence of a possible gravitationally lensed arc $\sim 13''$ northeast of the BCG.

5.14. PSZ2 G224.82+13.62

The BCG of this system is partially obscured by a nearby star and was not fully deblended in our catalogs. Still we are able to find a rich cluster at $z_{\text{cl}} = 0.24 \pm 0.04$ with 55 members. An interesting aspect of this cluster is that it is positionally coincident with an unidentified X-ray source (2E 0759.2–0355) from the *Einstein Observatory* (Harris et al. 1990). This cluster was confirmed by Barrena et al. (2018) with a spectroscopic redshift of $z_{\text{spec}} = 0.274$ from 28 members.

5.15. PSZ2 G305.76+44.79

Finally, PSZ2 G305.76+44.79 is our second highest redshift cluster at $z_{\text{cl}} = 0.72 \pm 0.07$ with at least 58 members. The BCG is associated with radio source PMN J1259–1801 with a 1.4 GHz flux density of 42.2 ± 1.4 mJy from the NVSS.

6. Discussion

In this section, we discuss the results given in the previous section as a whole, and frame those results in the context of the broader PSZ sample.

6.1. Overview of the Sample

Of the 85 cluster candidates observed as part of our program, we confirm 15 clusters, 12 of which were previously

unrecognized as associations with *Planck* candidates. The SNR range of our observed sample covers values 5.06–15.89 with a median value of 6.35. The sample of confirmed clusters has a considerably lower range of SNR values (5.51–7.87) with a lower median of 5.80. The clusters span the redshift range $0.13 < z < 0.78$ with mean redshift $\langle z \rangle = 0.36$. Seven of the clusters have published spectroscopic redshifts from other observations (see Section 5 for details). The scatter between our reported photo-z's and the reported spec-z's, using Equation (1), is $\sigma_f = 0.036$ indicating that our clusters' photometric redshifts are accurate.

As part of the confirmation process we limited our cluster search to objects within 6' of the reported PSZ position. The mean separation between our reported BCGs and the PSZ position is 2'.15 with 68% of BCGs within 2' of the quoted PSZ position. We find that our spatial distribution of clusters is roughly consistent with other follow-up observations of PSZ cluster candidates (e.g., Barrena et al. 2018).

A number of clusters have noteworthy properties. We find that roughly one-third of the confirmed sample appear to contain multiple BCGs, or are part of multicluster systems. Of the 15 clusters, 7 have BCGs or other cluster members that host radio sources.

6.2. Implications for Full PSZ Sample

Using our galaxy cluster identification scheme described in Section 4.3, we fail to identify an optical counterpart to 70 PSZ cluster candidates. Because our observations are limited to candidates with $\text{SNR} > 5\sigma$, we would expect at most one failed detection. Here we discuss three possible scenarios that could contribute to this low purity.

The first possibility is that clusters in our sample were missed because they are at low- z . The initial design of our survey restricts the cluster search to a 6' radius search window centered on the PSZ position. Low- z clusters could appear as an isolated elliptical galaxy or a small number of galaxies and thus might not be classified as clusters. A follow-up inspection of the full-sized mosaics, approximately 1 degree², reveals no such low- z structures.

To investigate this low- z hypothesis quantitatively, we compute the expected fraction of galaxy clusters as a function of redshift from the cluster mass function of Tinker et al. (2008). The cluster mass sensitivity of *Planck* varies with redshift (see Figure 27, Planck Collaboration et al. 2015a). To capture this variability, we draw random samples (with replacement) from the confirmed sample of clusters as reported in Planck Collaboration et al. (2015a). Because each cluster is previously confirmed, the PSZ2 catalog provides an M_{500c} estimate of the total mass. The bottom panel of Figure 4 shows the cluster mass as a function of redshift, where the gray lines are individual samples and the orange solid and dashed curves are the median and 68% limits respectively. The top panel of Figure 4 shows the expected cumulative distribution of galaxy clusters as a function of redshift.

From these numerical simulations we can see that a low fraction (<5%) of all clusters detectable by *Planck* are expected to reside at redshifts less than 0.1. Of the 85 fields observed, we expect approximately four clusters to lie at such low redshifts. This is consistent with the three low- z clusters we recover during the course of our analysis. Thus it is very unlikely that we have missed a significant number of low redshift clusters.

The second possibility posits that many of the clusters in our sample lie at redshifts beyond our optical detection limits. The median limiting *i*-band magnitude of our survey is 23.2 mag, corresponding to a limiting redshift of $z = 0.75$ for an L_* galaxy (see Figure 2).

From the predicted number of PSZ clusters as a function of redshift (Figure 4), we expect $\sim 3\%$ of the sample to lie at $z > 0.7$. Out of the 1943 total *Planck* SZ detections, our simulated redshift distribution predicts that there should be 58 clusters at high- z (if all *Planck* SZ detections are real clusters). There are only 12, currently confirmed, clusters at $z > 0.7$ in PSZ2, only 5 of which are above $z = 0.8$. So there should be 46 high- z clusters among the unconfirmed sample of 613, or approximately 7%. Applying this percentage to the 85 fields we observed, suggests that we should have found six high- z clusters. We have only found two, each of which lies close to the redshift limit of our optical search.

Thus while high- z systems were expected to be missed by this (optical only) survey, high- z clusters alone cannot account for the high number of *still-unconfirmed* clusters. We expect that further *follow-up* observations with deep infrared imaging will be required to either confirm or place additional limits on putative high- z clusters.

The third possibility is that the underlying cause for failed cluster identification is confusion from source crowding in our images. For example, if a cluster lies behind a dense foreground of unrelated sources, then it could be difficult to visually identify the BCG and the corresponding fainter, member galaxies. To estimate the object surface density in our fields, we sum the number of objects reported by SExtractor and divide by the sky-area of the image. Figure 5 allows us to explore the possibility that we fail to confirm a cluster in the majority of fields due to unrelated sources. The left panel shows the surface density of objects in the search area as a function of the limiting *i*-band magnitude (see also the left panel of Figure 2). The right panel shows the number of observed fields with the corresponding object density. In both panels, the fields where we do not identify a cluster are shown in blue, and the fields with successfully identified clusters are shown in orange.

Our identified clusters fall in a relatively narrow range of object densities, 10–30 objects arcmin $^{-2}$. Roughly *two-thirds* of our fields fall within this range. Of the 31 fields outside the range, 15 fields have higher densities. If all 15 fields contain an unidentified *cluster*, we could still not account for the vast majority of fields where we did not identify a cluster, 51 fields or $\sim 60\%$ of our observed sample.

Perhaps more interesting are the 16 fields where the object surface density is lower than the range where we made successful identifications. These are fields where it should be relatively easy to identify a massive cluster should it exist. Of course, the presence of a massive cluster could raise the object density above the lower identification threshold. These fields, especially the fields with deep optical limiting magnitudes are prime candidates for the potential high- z clusters lurking beyond the reach of our optical search.

An alternative to the above possibilities is that the vast majority of cluster candidates in our sample are not true 5σ (or higher) detections. In other words, no optical counterpart to the PSZ detection exists. One possibility for the low confirmation fraction is contamination of the *Planck* SZ signal by unrelated radio source emission. To investigate this, as part of our NED

search, we track NVSS radio sources within 5' of the reported PSZ position. We find approximately 75% of confirmed PSZ clusters have a NVSS radio source (39.6 mJy average flux) and unconfirmed PSZ candidates show slightly fewer sources with approximately 55% having a NVSS radio source (25.1 mJy average flux) within 5'. For the 85 cluster candidates observed in this work $\sim 70\%$ of fields have at least one radio source (30.8 mJy average flux). Of the 15 confirmed *clusters*, 12 (80%; 26.12 mJy average flux) have nearby radio sources. Based on these results, we find it unlikely that radio contamination is a leading cause of the low purity of the unconfirmed PSZ sample.

The search method we employed for this study has focused on identifying optically rich systems. This clearly assumes that the unconfirmed clusters are like previously confirmed clusters from *Planck*, SPT, and ACT. Although this is a fully justified assumption, it also means that we have potentially missed identifying a class of optically poorer clusters associated with the *Planck* candidates. Indeed the low identification fraction in our work suggests that many aspects of the confirmation process (optical band searches, restricting counterparts to a specified separation from the cataloged *Planck* position, requiring high optical richness for the counterparts, and so on) may need to be re-evaluated.

7. Summary

In this work, we report on our analysis of images targeting galaxy cluster candidates selected from the second *Planck* all-sky galaxy cluster catalog (PSZ2; *Planck* Collaboration et al. 2015a). We observe 85 candidates with SZ effect SNR > 5 over the course of 17 nights spread over three years (2014–2017). We independently develop and utilize a pipeline to process the *griz* imaging taken with both the MOSAIC 1.1 and MOSAIC 3 imagers on the KPNO Mayall-4 m telescope (see Section 3). We present the first results from the complete data set of 85 fields, 15 rich galaxy clusters of which 12 were previously unassociated with a *Planck* cluster.

After computing accurate photometric redshifts (see Section 4), we visually inspect each galaxy cluster candidate and adopt stringent confirmation criteria based on the richness and separation from the reported PSZ2 position.

The newly discovered clusters range in photometric redshift between $0.13 < z < 0.78$. The upper redshift limit is due to the depth of imaging restricting our ability to reliably detect L_* galaxies to $z < 0.9$. Ultimately, this prevents us from finding the most interesting rich clusters at very high redshifts; this will be addressed in a future follow-up study.

A large motivation for this work has come from the recent successes of other SZ follow-up programs (see citations in Section 1). We present this sample of clusters to aid in the confirmation of the full PSZ cluster sample, and to potentially reveal clusters with interesting astrophysical properties. The PSZ cluster *candidates*, which remain unconfirmed have the potential to be the most interesting.

In future work, we will continue to re-evaluate our confirmation methodology to explore the possibility that other lower, richness systems are potential *counterparts* to the *Planck* sample. Additionally, we expect a few higher redshift clusters in the sample of 85 included in this survey, and will explore this with *multiwavelength* studies.

The source code used to conduct this analysis is available at <https://github.com/boada/planckClusters>. The raw and

processed imaging along with final data products for the 15 clusters presented here are available upon request.

This work was supported by NASA Astrophysics Data Analysis grant number NNX14AF73G and NSF Astronomy and Astrophysics Research Program award number 1615657. L.F.B. acknowledges support from CONICYT project Basal AFB-170002. We thank the several undergraduate students who worked on this project: August Miller, Alexis Freiling, Jessica Kerman, Kevin Feigl, Ingrid Zimmerman, and Cole Bisaccia. Alexis, Jessica, and Ingrid were participants in Project SUPER (Science for Undergraduates: A Program for Excellence in Research), a STEM-focused enrichment program through Douglass that offers undergraduate women the opportunity to actively participate in academic research. August participated in the 2014 Rutgers NSF REU program. This research made use of several open-source packages: APLPY,¹⁰ an open-source plotting package for Python; the IPYTHON¹¹ package (Perez & Granger 2007); MATPLOTLIB¹², a Python library for publication quality graphics (Hunter 2007) and ASTROPY,¹³ a community developed core Python package for Astronomy (The Astropy Collaboration et al. 2013). Funding for the SDSS and SDSS-II has been provided by the Alfred P. Sloan Foundation, the Participating Institutions, the National Science Foundation, the U.S. Department of Energy, the National Aeronautics and Space Administration, the Japanese Monbukagakusho, the Max Planck Society, and the Higher Education Funding Council for England. The SDSS is managed by the Astrophysical Research Consortium for the Participating Institutions. This work has made use of data from the European Space Agency (ESA) mission *Gaia*,¹⁴ processed by the *Gaia* Data Processing and Analysis Consortium¹⁵ (DPAC). Funding for the DPAC has been provided by national institutions, in particular, the institutions participating in the *Gaia* Multilateral Agreement. This research has made use of the VizieR catalog access tool, CDS, Strasbourg, France. The original description of the VizieR service was published in Ochsenbein et al. (2000). This research has made use of the SVO Filter Profile Service¹⁶ supported from the Spanish MINECO through grant AyA2014-55216. This research has made use of the NASA/IPAC Extragalactic Database (NED), which is operated by the Jet Propulsion Laboratory, California Institute of Technology, under contract with the National Aeronautics and Space Administration. Finally, we thank all the staff at KPNO for ensuring the success of our observing and aiding in the acquisition of our data.

ORCID iDs

Steven Boada  <https://orcid.org/0000-0002-0307-8693>
 John P. Hughes  <https://orcid.org/0000-0002-8816-6800>
 Peter Doze  <https://orcid.org/0000-0002-2408-0813>
 L. Infante  <https://orcid.org/0000-0001-8581-932X>

¹⁰ <http://aply.github.com>

¹¹ <https://ipython.org>

¹² <https://matplotlib.org>

¹³ <http://www.astropy.org>

¹⁴ <https://www.cosmos.esa.int/gaia>

¹⁵ <https://www.cosmos.esa.int/web/gaia/dpac/consortium>

¹⁶ <http://svo2.cab.inta-csic.es/theory/fps/>

References

- Abell, G. O. 1958, *ApJS*, 3, 211
 Aihara, H., Arimoto, N., Armstrong, R., et al. 2018, *PASJ*, 70, arXiv:1704.05858
 Albareti, F. D., Prieto, C. A., Almeida, A., et al. 2017, *ApJS*, 233, 25
 Amodeo, S., Mei, S., Stanford, S. A., et al. 2018, *ApJ*, 853, 36
 Barrena, R., Streblyanska, A., Ferragamo, A., et al. 2018, *A&A*, 616, A42
 Bauer, F. E., Condon, J. J., Thuan, T. X., & Broderick, J. J. 2000, *ApJS*, 129, 547
 Becker, R. H., White, R. L., & Helfand, D. J. 1995, *ApJ*, 450, 559
 Benitez, N. 2000, *ApJ*, 536, 571
 Bertin, E. 2006, in ASP Conf. Ser. 351, Astronomical Data Analysis Software and Systems XV, ed. C. Gabriel et al. (San Francisco, CA: ASP), 112
 Bertin, E., & Arnouts, S. 1996, *A&AS*, 117, 393
 Bertin, E., & Emmanuel 2011, Astrophysics Source Code Library, record  ascl:1110.006
 Bertin, E., Mellier, Y., Radovich, M., et al. 2002, in ASP Conf. Ser. 281, Astronomical Data Analysis Software and Systems XI, ed. D. Bohlander, D. Durand, & T. Handley (San Francisco, CA: ASP), 228
 Blanton, M. R., Hogg, D. W., Bahcall, N. A., et al. 2003, *ApJ*, 592, 819
 Bleem, L. E., Stalder, B., de Haan, T., et al. 2015, *ApJS*, 216, 27
 Böhringer, H., Voges, W., Huchra, J. P., et al. 2000, *ApJS*, 129, 435
 Borgani, S., Rosati, P., Tozzi, P., et al. 2001, *ApJ*, 561, 13
 Brown, A. G. A., Vallenari, A., Prusti, T., et al. 2016, *A&A*, 595, A2
 Bruzual, G., & Charlot, S. 2003, *MNRAS*, 344, 1000
 Burenin, R. A. 2017, *AstL*, 43, 507
 Calvi, V., Stiavelli, M., Bradley, L., Pizzella, A., & Kim, S. 2014, *ApJ*, 796, 102
 Carlstrom, J. E., Ade, P. A. R., Aird, K. A., et al. 2011, *PASP*, 123, 568
 Chabrier, G. 2003, *PASP*, 115, 763
 Chambers, K. C., Magnier, E. A., Metcalfe, N., et al. 2016, arXiv:1612.05560
 Coe, D., Benitez, N., Sanchez, S. F., et al. 2006, *AJ*, 132, 926
 Condon, J. J., Cotton, W. D., Greisen, E. W., et al. 1998, *AJ*, 115, 1693
 Dahle, H., Pedersen, K., Lilje, P. B., Maddox, S. J., & Kaiser, N. 2003, *ApJ*, 591, 662
 Dahlen, T., Mobasher, B., Faber, S. M., et al. 2013, *ApJ*, 775, 93
 Dark Energy Survey Collaboration, Abbott, T., Abdalla, F. B., et al. 2016, *MNRAS*, 460, 1270
 de Vaucouleurs, G. 1948, *AnAp*, 11, 247
 Donahue, M., Voit, G. M., Gioia, I., et al. 1998, *ApJ*, 502, 550
 Douglas, J. N., Bash, F. N., Bozian, F. A., Torrence, G. W., & Wolfe, C. 1996, *AJ*, 111, 1945
 Ebeling, H., Edge, A. C., Böhringer, H., et al. 1998, *MNRAS*, 301, 881
 Eke, V. R., Cole, S., & Frenk, C. S. 1996, *MNRAS*, 282, 263
 Evrard, A. E. 1989, *ApJ*, 341, L71
 Flewelling, H. A., Magnier, E. A., Chambers, K. C., et al. 2016, arXiv:1612.05243
 Gioia, I. M., Maccacaro, T., Schild, R. E., et al. 1990, *ApJS*, 72, 567
 Harris, D. E., Forman, W., Gioia, I. M., et al. 1990, in The Einstein Observatory Catalog of IPC X-ray Sources. Volume 4E: Right Ascension Range 08h 00m to 11h 59m, ed. D. E. Harris et al. (Smithsonian Astrophysical Observatory), 4
 Harrison, I., & Coles, P. 2012, *MNRAS: Letters*, 421, L19
 Harrison, I., & Hotchkiss, S. 2013, *JCAP*, 2013, 022
 Hasselfield, M., Hilton, M., Marriage, T. A., et al. 2013, *JCAP*, 2013, 008
 Henry, J. P. 2004, *ApJ*, 609, 603
 Henry, J. P., & Arnaud, K. A. 1991, *ApJ*, 372, 410
 Hilton, M., Hasselfield, M., Sifón, C., et al. 2018, *ApJS*, 235, 20
 Høg, E., Fabricius, C., Makarov, V. V., et al. 2000, *A&A*, 355, L27
 Huchra, J. P., Geller, M. J., Henry, J. P., & Postman, M. 1990, *ApJ*, 365, 66
 Hunter, J. D. 2007, *CSE*, 9, 90
 Ilbert, O., Capak, P., Salvato, M., et al. 2009, *ApJ*, 690, 1236
 Jenkins, A., Frenk, C. S., White, S. D. M., et al. 2001, *MNRAS*, 321, 372
 Koester, B. P., McKay, T. A., Annis, J., et al. 2007, *ApJ*, 660, 239
 Kron, R. G. 1980, *ApJS*, 43, 305
 Liu, J., Hennig, C., Desai, S., et al. 2015, *MNRAS*, 449, 3370
 LSST Dark Energy Science Collaboration 2012, 133, arXiv:1211.0310
 Mantz, A., Allen, S. W., Ebeling, H., & Rapetti, D. 2008, *MNRAS*, 387, 1179
 Marriage, T. A., Acquaviva, V., Ade, P. A. R., et al. 2011, *ApJ*, 737, 61
 Menanteau, F., González, J., Juin, J.-B., et al. 2010a, *ApJ*, 723, 1523
 Menanteau, F., Hughes, J. P., Barrientos, L. F., et al. 2010b, *ApJS*, 191, 340
 Menanteau, F., Hughes, J. P., Jimenez, R., et al. 2009, *ApJ*, 698, 1221
 Menanteau, F., Hughes, J. P., Sifón, C., et al. 2012, *ApJ*, 748, 7
 Menanteau, F., Sifón, C., Barrientos, L. F., et al. 2013, *ApJ*, 765, 67
 Michel, A., & Huchra, J. 1988, *PASP*, 100, 1423

- Molino, A., Benítez, N., Ascaso, B., et al. 2017, *MNRAS*, **470**, 95
 Mommert, M. 2017, *A&C*, **18**, 47
 Mortonson, M. J., Hu, W., & Huterer, D. 2010, *PhRvD*, **83**, 023015
 Ochsenbein, F., Bauer, P., & Marcout, J. 2000, *A&AS*, **143**, 23
 Oke, J. B. 1974, *ApJS*, **27**, 21
 Perez, F., & Granger, B. E. 2007, *CSE*, **9**, 21
 Planck Collaboration, Ade, P. A. R., Aghanim, N., et al. 2011, *A&A*, **536**, A1
 Planck Collaboration, Ade, P. A. R., Aghanim, N., et al. 2014, *A&A*, **571**, A29
 Planck Collaboration, Ade, P. A. R., Aghanim, N., et al. 2015a, *A&A*, **594**, A27
 Planck Collaboration, Ade, P. A. R., Aghanim, N., et al. 2015b, *A&A*, **582**, A29
 Planck Collaboration, Ade, P. A. R., Aghanim, N., et al. 2016, *A&A*, **586**, A139
 Postman, M., Lubin, L. M., Gunn, J. E., et al. 1996, *AJ*, **111**, 615
 Prusti, T., de Bruijne, J. H. J., Brown, A. G. A., et al. 2016, *A&A*, **595**, A1
 Schlegel, D. J., Finkbeiner, D. P., & Davis, M. 1998, *ApJ*, **500**, 525
 Streblyanska, A., Barrena, R., Rubiño-Martín, J. A., et al. 2018, *A&A*, **617**, A71
Q6
 Smelev, R. A., & Zeldovich, Y. B. 1972, *CoASP*, **4**
 Swetz, D. S., Ade, P. A. R., Amiri, M., et al. 2011, *ApJS*, **194**, 41
 Tauber, J. A., Mandolesi, N., Puget, J.-L., et al. 2010, *A&A*, **520**, A1
 The Astropy Collaboration, Robitaille, T. P., Tollerud, E. J., et al. 2013, *A&A*, **558**, A33
 The Dark Energy Survey Collaboration 2005, 42, arXiv:[astro-ph/0510346](https://arxiv.org/abs/astro-ph/0510346)
 Tinker, J., Kravtsov, A. V., Klypin, A., et al. 2008, *ApJ*, **688**, 709
 Tody, D. 1993, *adass* II, 52
 Valdes, F. G., & Swaters, R. A. 2007, in *ASP Conf. Ser.* 376, *Astronomical Data Analysis Software and Systems XVI*, ed. R. Shaw, F. Hill, & D. Bell (San Francisco, CA: ASP), 273
 van der Burg, R. F. J., Aussel, H., Pratt, G. W., et al. 2016, *A&A*, **587**, A23
 Vanderlinde, K., Crawford, T. M., de Haan, T., et al. 2010, *ApJ*, **722**, 1180
 Vikhlinin, A., Kravtsov, A. V., Burenin, R. A., et al. 2009, *ApJ*, **692**, 1060
 Voges, W., Aschenbach, B., Boller, T., et al. 1999, *A&A*, **349**, 389
 Voges, W., Aschenbach, B., Boller, T., et al. 2000, *IAU Circulars*, 7432
 Waizmann, J.-C., Ettori, S., & Bartelmann, M. 2013, *MNRAS*, **432**, 914
 Wen, Z. L., Han, J. L., & Yang, F. 2018, *MNRAS*, **475**, 343
 Wenger, M., Ochsenbein, F., Egret, D., et al. 2000, *A&AS*, **143**, 9
 White, S. D. M., Efstathiou, G., & Frenk, C. S. 1993a, *MNRAS*, **262**, 1023
 White, S. D. M., Navarro, J. F., Evrard, A. E., & Frenk, C. S. 1993b, *Natur*, **366**, 429
 Wittman, D., Dell'Antonio, I. P., Hughes, J. P., et al. 2006, *ApJ*, **643**, 128
 York, D. G., Adelman, J., Anderson, John, E. J., et al. 2000, *AJ*, **120**, 1579
 Zwicky, F., & Kowal, C. T. 1968, *Catalogue of Galaxies and of Clusters of Galaxies*, Vol. VI (Pasadena, CA: California Institute of Technology)